

See discussions, stats, and author profiles for this publication at: <https://www.researchgate.net/publication/267308800>

333052 CO₂ Utilization Via Chemical Looping Process

CONFERENCE PAPER · NOVEMBER 2013

READS

50

3 AUTHORS:



Vladimir Galvita

Ghent University

63 PUBLICATIONS 897 CITATIONS

SEE PROFILE



H. Poelman

Ghent University

101 PUBLICATIONS 1,798 CITATIONS

SEE PROFILE



Bryan Marin

Ghent University

403 PUBLICATIONS 4,844 CITATIONS

SEE PROFILE

CeO₂-Modified Fe₂O₃ for CO₂ Utilization via Chemical Looping

Vladimir V. Galvita,^{*,†} Hilde Poelman,[†] Vitaliy Bliznuk,[‡] Christophe Detavernier,[§] and Guy B. Marin[†]

[†]Laboratory for Chemical Technology, Ghent University, Krijgslaan 281 (S5), B-9000 Gent, Belgium

[‡]Department of Materials Science and Engineering, Ghent University, Technologiepark 903, 9052 Zwijnaarde, Ghent, Belgium

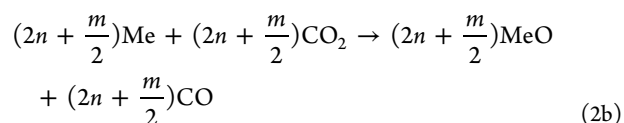
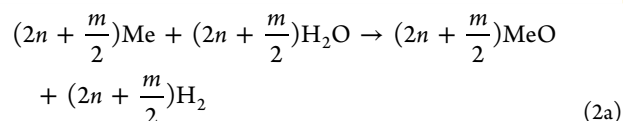
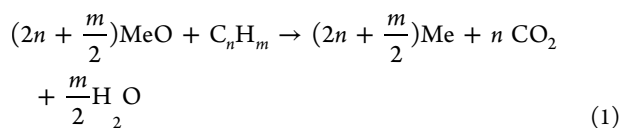
[§]Department of Solid State Sciences, Ghent University, Krijgslaan 281, S1, B-9000 Ghent, Belgium

ABSTRACT: Both pure and mixed CeO₂–Fe₂O₃ were prepared for CO₂ reduction to CO by chemical looping. The crystallographic structure of the investigated materials was monitored in situ during H₂ reduction and CO₂ oxidation. A solid solution of iron in ceria was identified. Up to 70 wt % CeO₂, a distinct Fe₂O₃ hematite phase occurred next to the solid solution. At higher CeO₂ content, no diffraction patterns corresponding to iron oxide phases were present, but upon H₂ temperature programmed reduction, a metal iron phase appeared. The Fe₂O₃ phase at lower CeO₂ content, during H₂ temperature programmed reduction, completely reduced at 700 °C while the solid solution was only partially reduced. For all investigated samples, CO₂ reoxidized iron in one-step to Fe₃O₄ from 500 °C during temperature programmed oxidation. Adding CeO₂ to Fe₂O₃ was beneficial for the materials activity and stability. Isothermal redox cycles were performed without significant loss of CO₂ conversion. The highest CO yield was obtained for 20 wt % CeO₂–Fe₂O₃, but 50 and 70 wt % CeO₂–Fe₂O₃ were the most stable combinations.

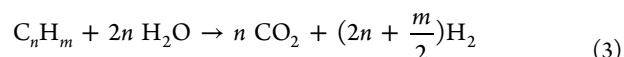
1. INTRODUCTION

To tackle the problem of increasing carbon dioxide concentration in the atmosphere, a key midterm strategy is the carbon dioxide capture, transformation, and storage.¹ Chemical looping (CL) is one of several emerging technology options capable of reducing the carbon dioxide emissions and helping in a diverse range of applications for production of fuels, chemicals, and electricity.^{2–4} In a general chemical looping process, a metal oxide (MeO) is circulated between two reactors: the reducer and oxidizer. If chemical looping is applied as a combustion process (CLC = chemical looping combustion), MeO reacts in the reducer with the fuel to produce CO₂ and H₂O, leaving metal (Me) or metal oxide in a reduced state.² In the oxidizer, it is reoxidized to its initial state with air. Thus, fuel and air never mix, and CO₂ is not diluted by nitrogen, which is important for the carbon dioxide sequestration process.

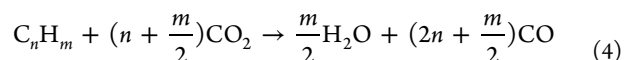
Other chemical looping schemes have been devised to produce hydrogen or synthesis gas rather than heat or power.^{2,5–12} Chemical looping steam (CLSR) or dry reforming (CLDR) processes utilize the same basic principles as chemical looping combustion (CLC).¹³ In these processes, the fuel is again completely oxidized over the metal oxides (eq 1). The difference is that now the H₂O or CO₂ product is used as an oxidant instead of air. The outlet from the looping reactor then consists of H₂ or CO, eqs 2a or 2b, respectively, which can be used as feedstock for chemical processes.



Steam reforming, eqs 1 + 2a, proceeds as:



while the overall dry reforming reaction, eqs 1 + 2b, runs as:



Typical challenges with current dry reforming technologies are catalyst cost and their deactivation due to coking, as well as product selectivity. However, the present CLDR process differs significantly from conventional catalytic dry reforming processes. While the target of conventional dry reforming is high syngas yield, CLDR is here optimized for CO₂ activation. Equation 4 indicates that such process utilizes more carbon dioxide (eq 2b) than it produces in the reduction step (eq 1). In the case of CH₄, the process can convert four times as much as CO₂ than is produced. If in addition the reactor can be heated using solar energy as external heat source, this process can be made highly efficient.

A proof of principle of the CLDR concept was presented by Najera et al.¹³ The authors evaluate the potential of CLDR

Received: January 30, 2013

Revised: May 16, 2013

Accepted: May 30, 2013

Published: May 30, 2013

through a combination of thermodynamic calculations for carrier selection, synthesis, and characterization of highly active and high-temperature stable nanostructured oxygen carriers, and a brief reactor modeling study to evaluate process feasibility in a periodically operated fixed-bed reactor.¹³

A key issue in CLDR processes is the selection of an appropriate oxygen carrier material. The reactivity of the oxygen storage material, its cost, and thermal stability are critical selection criteria. A broad range of metals was analyzed to determine the thermodynamic equilibrium limitations for redox cyclic processes.^{7,9,13,14} While a number of metals/metal oxides (Mo, Cr, Zn, Co, Nb, Ce) give reasonable CO₂ reduction capacity, it is apparent that only iron yields high oxygen storage capacity from CO₂ (0.7 mol CO₂/mol Fe) over a wide range of operating temperatures (600–1800 °C).

Thus, the chemical looping conversion of CO₂ into CO over iron oxide as oxygen storage material has been one of the possible target technologies for CO₂ utilization. The ability of the oxygen storage material to maintain its high activity in repeated reduction/reoxidation cycles is the most critical issue for the overall economic viability of the CO₂ splitting process. Loutzenhiser et al. showed that CO₂ gas splitting by reaction with FeO particles depends strongly on surface area and attributed this to a rate-limiting surface chemical reaction.¹⁵ However, it is well-known that iron oxides with high surface area rapidly deactivate due to material sintering,¹⁶ which is a largely irreversible process. The further optimization of the process requires prevention of sintering of the iron oxide during redox cycles and increasing its reactivity. Such activity improvement of the oxygen storage material will increase the feasibility of the CO₂ splitting process by means of CLDR in comparison to other traditional technologies.

In an effort to eliminate sintering problems that effectively shut down the gas splitting reaction, ferrites deposited on porous supports such as TiO₂, SiO₂, Al₂O₃, ZrO₂, CeO₂, CeZrO₂, and/or ferrites promoted by different metal additives were proposed by several investigators.^{16–20} Among those materials, cerium oxide stands out as it has high activity in methane or syngas oxidation by lattice oxygen,^{21–23} as well as reasonable CO₂ reoxidation capacity^{24,25} in parallel to the iron oxide:



The redox couple Ce⁴⁺ and Ce³⁺ facilitates oxygen storage and release from its bulk fluorite lattice.²⁶ Additionally, cerium oxide induces structural modification and stabilization of iron oxides, making it an ideal candidate for promoting iron oxide in a chemical looping process. The formation of a solid solution between MeO (Me = Mn, Fe, or Cu) and CeO₂ has been found to be effective for the enhancement of reducibility at lower temperatures compared with pure CeO₂.^{18,27–29}

The objective of the present study is to investigate the CO₂ reoxidation efficiency of a series of CeO₂–Fe₂O₃ mixed oxides prepared by coprecipitation for the utilization of CO₂ in a chemical looping process. Hence, experimental performance data are reported as well as structural characterization of the oxygen storage materials during reduction and CO₂ reoxidation. In addition, the stability of performance was tested through prolonged use of the material.

2. MATERIALS AND SETUP

2.1. Materials Preparation. Samples with 0, 20, 50, 70, 90, and 100 wt % of CeO₂ in CeO₂–Fe₂O₃ were investigated. The

following chemicals were used in the preparation of the mixed oxides: Fe(NO₃)₃·9H₂O (99.99+%, Sigma-Aldrich) and Ce(NO₃)₃·6H₂O (99.99%, Sigma-Aldrich). Samples were prepared by coprecipitation by adding an excess of ammonium hydroxide. This mixture was kept at room temperature for 24 h. Hereafter, the sample was separated as precipitate from the solution, washed with ethanol, and dried overnight in an oven at 383 K. Finally, the materials were calcined at 1023 K. The resulting samples were labeled as xCe-Fe, with *x* standing for the CeO₂ wt % in the sample.

2.2. General Characterization. The Brunauer–Emmett–Teller (BET) surface area was determined by N₂ adsorption at 77 K (five point BET method using Gemini Micromeritics). Prior to analysis, the sample was outgassed at 300 °C for 6 h to eliminate volatile adsorbates from the surface. The crystallographic phase of the materials as prepared was determined using a Siemens Diffractometer Kristalloflex D5000, with Cu K α radiation. The powder patterns were collected in a 2 θ range from 10° to 80° with a step of 0.02° and 30 s counting time per angle. By fitting a Gaussian function to a diffraction peak, the crystallite size can be determined from the peak width via the Scherrer equation,³⁰ while the peak position gives information about the lattice spacing based on the Bragg law of diffraction: $2d\sin(\theta) = n\lambda$.³¹

Morphological, structural, and local chemical analyses were carried out by means of transmission electron microscopy (TEM)-based methods: high resolution (HRTEM), scanning transmission bright field (STEM BF), selected area electron diffraction (SAED), energy dispersive X-ray spectrometry (EDX), and electron energy-loss spectrometry (EELS). A microscope JEOL JEM-2200FS, Cs-corrected, operated at 200 kV and equipped with Schottky-type field-emission gun (FEG), EDX JEOL JED-2300D and JEOL in-column omega filter (EELS), was used. Specimens were prepared by immersion of a lacey carbon film on a copper support grid into the as prepared powder. Particles sticking to the carbon film were investigated. A beryllium specimen retainer was used to eliminate secondary X-ray fluorescence in EDX spectra originating from the specimen holder.

The redox behavior of the different samples was investigated using H₂-TPR and CO₂-TPO (Autochem II 2920, Micromeritics). About 20 mg of sample was pretreated in a He stream at 600 °C for 30 min prior to running the TPR experiment and then cooled to room temperature in He. A feed of 5% H₂ in helium at a flow rate of 0.02 mol/s was used as reducing gas. Prior to CO₂-TPO, the xCe-Fe samples were reduced in 5% H₂/He during 30 min at 750 °C. CO₂ at a flow rate of 0.02 mol/s was used as oxidizing gas. For both TPR and TPO, the temperature was ramped at a constant rate of 20 °C/min. The CO₂ and H₂ consumption were monitored by MS (OmniStar, Pfeiffer Vacuum).

To test reactivity and stability of the xCe-Fe materials, experiments were conducted in a fixed-bed reactor at 600 °C using hydrogen as model fuel. This fuel was chosen to avoid carbon formation as when feeding methane and, hence, to focus on the oxidation of the chemical looping material using CO₂ as an oxidant as well as on the stability of the material in cyclic redox operation.

2.3. In Situ Time-Resolved XRD. Crystallographic analyses for the tested catalysts were performed by means of in situ X-ray diffraction (XRD) measurements in θ –2 θ mode using a Bruker-AXS D8 Discover apparatus with Cu K α radiation of wavelength 0.154 nm and a linear detector covering

a range of 20° in 2θ with an angular resolution of approximately 0.1° 2θ . While the minimal capturing time is 0.1 s, a collection time of typically 10 s was used during these experiments.

The evolution of the catalyst structure during TPR or TPO was investigated in a flowing gas stream (5 vol.% H_2/He or CO_2) from room temperature to 800°C . The in situ experiments were carried out using a home-built reactor chamber with Kapton foil window for X-ray transmission. A 10 mg sample was evenly spread in a shallow groove of a single crystal Si wafer. Interaction of the catalyst material with the Si holder was never observed. The chamber atmosphere was pumped and flushed with a rotation pump (base pressure $\sim 4 \times 10^{-2}$ mbar) before introducing the reducing gas flow. The sample was heated from room temperature to 800°C at a heating rate of $20^\circ\text{C}/\text{min}$. In situ XRD during CO_2 -TPO immediately followed upon H_2 -TPR. Eventually, all samples were monitored with in situ XRD during an isothermal cycling procedure at 600°C . The latter consisted of 5×20 min cycles, where 5 min H_2 reduction was alternated with 5 min CO_2 reoxidation, always having 5 min He purging in between. Peak positions and widths were determined by means of a Gaussian function, fit to a XRD peak in a chosen range of 2θ around the peak of interest. Due to the low angular resolution of the linear detector, these values cannot yield accurate crystallite size and unit cell parameters, but they did allow tracing trends in a qualitative way.

2.4. Experimental Reaction Setup and Procedures.

Activity measurements were carried out at atmospheric pressure in a quartz tube microreactor (i.d. 10 mm), placed in an electric furnace. Typically, 100 mg of sample was packed between quartz wool plugs. The samples were diluted by quartz with a ratio of 1:5. The temperature of the catalyst bed was measured with K-type thermocouples touching the outside and inside of the reactor at the position of the catalyst bed. In all experiments, the material was reduced by hydrogen and reoxidized by CO_2 . The total flow rate of the feed gas into the reactor was maintained constant at 45 mmol/s by means of Brooks mass flow controllers. The activity of the prepared samples was investigated at 873 K. The feed and product gas streams were monitored online using MS. The response of the mass spectrometer detector was regularly verified with calibration gases. A carbon balance with a maximum deviation of 15% was obtained. As shown in a previous publication,¹⁶ the largest decrease in activity occurs during the first 10 redox cycles. Therefore, in order to assess stability of the samples, a series of 10 redox cycles was performed on each. Experiments were repeated 3 times independently in order to obtain standard deviations.

3. RESULTS AND DISCUSSION

3.1. Ex Situ XRD and BET. The as prepared materials were characterized by means of powder XRD to determine the crystalline phases (Figure 1). No Fe_2O_3 diffractions are present in the 90Ce–Fe pattern, which only shows the main CeO_2 peaks at $2\theta = 28.6^\circ$ (111) and 33.1° (200). For 70Ce–Fe, a clear contribution from Fe_2O_3 appears in XRD with peaks at 33.2° (104), overlapping with CeO_2 (200), and 35.6° (110). As the content of Fe_2O_3 increases, the Fe_2O_3 peaks intensify. The peaks of CeO_2 (111) and Fe_2O_3 (110) were used to determine the crystallite size from the peak width by means of the Scherrer equation. The pure materials CeO_2 (100Ce–Fe) and Fe_2O_3 (0Ce–Fe) have a crystallite size of 40 ± 5 and 200 ± 100 nm, respectively (Figure 2). Upon mixing of CeO_2 and

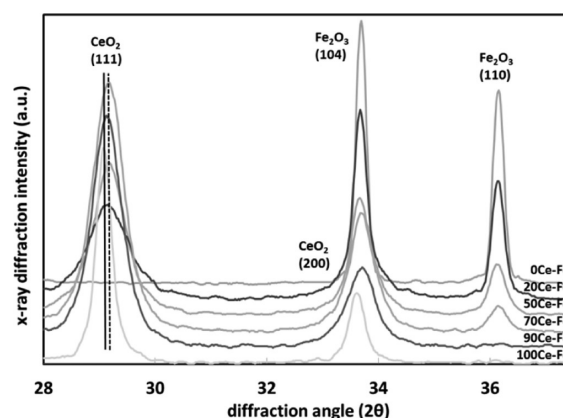


Figure 1. Powder diffraction patterns for the as prepared samples, 0Ce–Fe to 100Ce–Fe. The solid line indicates the position of the CeO_2 (111) diffraction for the pure compound, while the dashed line marks the position upon adding Fe_2O_3 to the material.

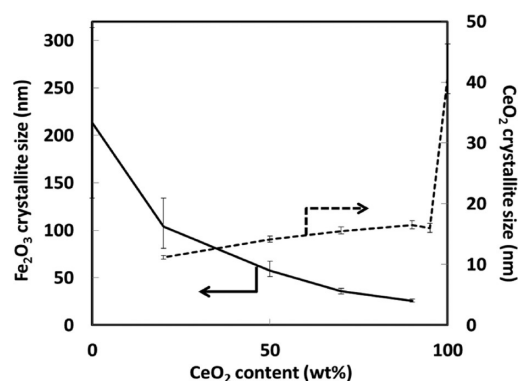


Figure 2. Crystallite size for Fe_2O_3 (solid line) and CeO_2 (dashed line) for increasing CeO_2 content as determined from peak width in powder diffraction patterns.

Fe_2O_3 , the crystallite size for ceria is reduced to less than half, and it remains at this lower value for further decreasing CeO_2 content. The interaction with Fe_2O_3 thus induces the formation of smaller ceria crystallites, possibly due to reduced sintering upon calcination of the material. For the Fe_2O_3 diffractions, the size of the crystallites increases gradually with relative Fe_2O_3 loading, from about 25 nm for 70Ce–Fe to over 100 nm for the 20Ce–Fe sample. All crystallite sizes are combined in Table 1.

From the peak position of CeO_2 (111), the unit cell parameter was determined following Bragg's law (Table 1). For 100Ce–Fe, a value of 0.5403 ± 0.0004 nm is obtained, which is slightly lower than the 0.5411 nm for bulk ceria.^{32,33} Upon mixing with Fe_2O_3 , the CeO_2 (111) diffraction shifts to higher diffraction angle (Figure 1), so that the unit cell parameter drops to around 0.5391 ± 0.0004 nm. This decrease can be induced by the incorporation of Fe^{3+} cations into the CeO_2 lattice. As the Fe^{3+} cation is smaller than the Ce^{4+} , 0.64 vs 1.01 Å, such incorporation causes the lattice to contract.^{28,32} As to the unit cell of Fe_2O_3 , lattice parameters a and c close to bulk values are found for all mixed samples. Table 1 summarizes the BET surface areas of the prepared series of samples. Pure 100Ce–Fe and 0Ce–Fe have a lower BET surface area than mixed CeO_2 – Fe_2O_3 , in agreement with their larger crystallite size.

3.2. TEM. TEM images of the 90, 70, 50, and 20Ce–Fe samples are shown in Figures 3–6. For the 90Ce–Fe sample,

Table 1. Surface Area, Fe₂O₃ and CeO₂ Crystallite Sizes, and Lattice Parameter of CeO₂ in Ce–Fe Samples^a

sample	surface areas (m ² /g)		crystallite size (nm)		lattice parameter CeO ₂ (nm)	
	fresh	used	Fe ₂ O ₃	CeO ₂ ^b	HRTEM	XRD
100Ce–Fe	9.1	8.5	— ^c	40.6	0.5411 ^d	0.5403 ± 0.0004
90Ce–Fe	18.0	12.9	— ^c	16.5	0.5270 ± 0.08	0.5393 ± 0.0004
70Ce–Fe	14.0	11.4	35.8	15.5	0.5271 ± 0.08	0.5389 ± 0.0004
50Ce–Fe	14.8	13.1	57.3	14.1	0.5172 ± 0.08	0.5386 ± 0.0004
20Ce–Fe	14.8	12.0	103.8	11.1	0.5110 ± 0.07	0.5389 ± 0.0004
0Ce–Fe	10.0	6.0	200	—	—	—

^aAfter 10 redox cycles. ^b(111). ^cNo diffraction peak present. ^dLiterature value.^{32,33}

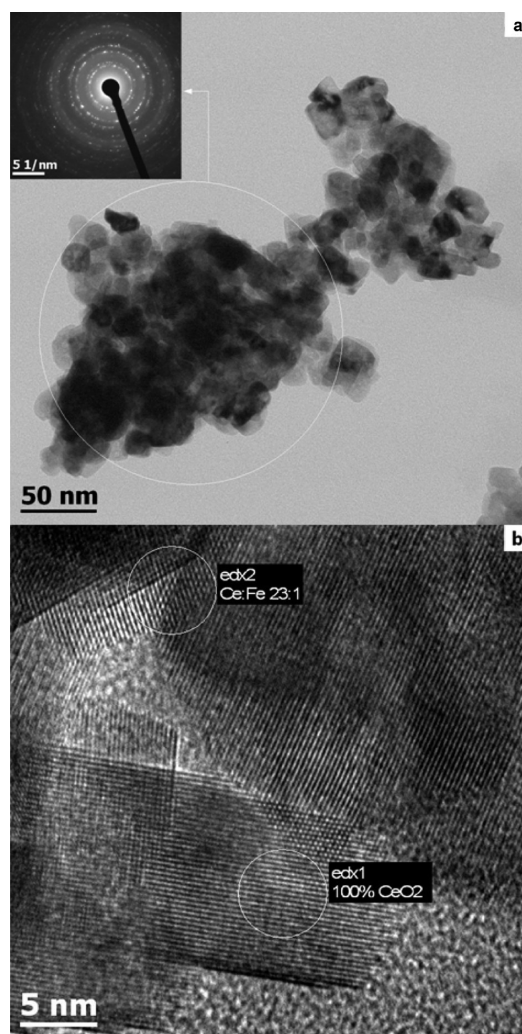


Figure 3. TEM-based results of 90Ce–Fe: (a) STEM BF image and SAED taken from the area within the circle; diffraction from CeO₂ detected only; (b) HRTEM image with EDX elemental data taken from within 5 nm circles showing pure CeO₂ (area edx1) and iron doped CeO₂ (area edx2, Ce/Fe 23:1).

the HRTEM micrograph shows all crystallites of similar morphology with size ~20 nm (Figure 3a). An SAED pattern for this sample, taken from within the 200 nm circled area of the figure, consists of ring shaped patterns with a discrete number of spots. The distances correspond to the lattice of ceria with $a = 0.527$ nm. SAED shows no evidence for the presence of crystalline iron oxide, which confirms the absence of Fe₂O₃ peaks in the XRD pattern. EDX spectra taken from within 5 nm circles in HRTEM images show the elemental

presence of cerium and oxygen (Figure 3b, edx1) and in some frames also of iron (Figure 3b, edx2). In the latter, the ratio of Ce to Fe was 23:1. FFT analysis from within both EDX areas yields a lattice parameter of 0.538 nm. These EDX results indicate that some Fe is present and could well be located within the ceria lattice, which could then account for its reduced lattice parameter.

The 70Ce–Fe sample displays a similar morphology (Figure 4a,b), and SAED confirms the presence of crystalline ceria with a lattice parameter of 0.527 nm. Although the XRD pattern contains peaks for crystalline Fe₂O₃, SAED measurements on this sample could not confirm this presence. EDX spectra show the elemental presence of iron, with an average atomic ratio of Ce to Fe within the ceria of 11:1. Further increasing the amount of iron oxide to 50 wt % leads to a partial separation of the two oxides (Figure 5a,b). In 50Ce–Fe, all crystallites present a similar morphology and average size around 20 nm. EDX now shows regions with clear Ce prevalence with Ce/Fe ratio of about 13:1 and lattice parameter of 0.517 nm, next to areas with a 1:1 Ce/Fe content and parts where the Fe signal dominates (Figure 5b). The atomic ratio of Ce to Fe in the Fe-rich areas amounts to 0.25:1. The addition of more Fe₂O₃ in the synthesis hence leads to crystallites with a variety of Ce/Fe ratios, existing next to each other. For the 20Ce–Fe sample, two different morphologies are observed: nanocrystals of ceria (~8 nm) are well dispersed over crystallites of Fe₂O₃ with estimated diameter of 60 nm; see Figure 6a,b. The inset of Figure 6b shows EELS with both Fe L and Ce M loss lines. The lattice parameter for the ceria nanocrystallites is 0.510 nm (see FFT inset in Figure 6b), and the average atomic ratio of Ce to Fe is 5:1. Table 1 presents the lattice parameters for the series of freshly prepared samples as determined by HRTEM. The lattice parameter for bulk CeO₂ is $a = 0.5411$ nm.^{32,33} For mixed samples, a contraction is evident from the unit cell parameter: ~0.527 to 0.510 nm (see Table 1). Previously, it was reported²⁸ that the Ce–Fe interaction occurred through formation of cubic ceria solid solutions where the Fe cations dissolve in the ceria structure. Because the Fe³⁺ cation (0.64 Å) and the Ce⁴⁺ cation (1.01 Å) have different ionic sizes, any cationic substitution will lead to contraction of the unit cell and a corresponding decrease in the lattice parameter. Thus, TEM visualizes a gradual evolution of the samples' morphology upon increasing amount of CeO₂ added to Fe₂O₃. Hence, in all mixed samples, a solid solution phase of Fe species incorporated into CeO₂ is present which forms the main difference with a 0Ce–Fe or 100Ce–Fe sample. For the smaller CeO₂ loadings, a separate Fe₂O₃ is formed. Thus, the XRD, EDX, SAED, EELS, and HRTEM results give rise to a Ce–Fe mixed material picture as drawn in Figure 7. The drawing illustrates the evolution of the Ce–Fe structure as a function of composition.

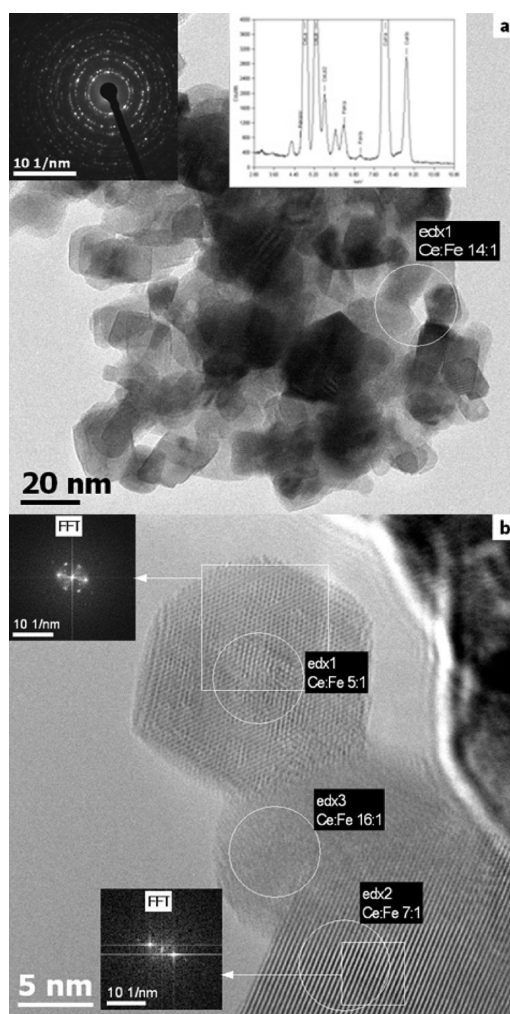


Figure 4. TEM-based study of 70Ce-Fe: (a) STEM BF image and EDX elemental data taken from the area within the circle; the SAED pattern is taken from a 200 nm diameter area, covering the whole agglomerate shown in the image; (b) HRTEM image of the agglomerate edge with FFTs, taken from the squared areas, and EDX elemental ratios taken from the circled areas.

3.3. Reactivity and Stability Tests. In order to test activity and stability of the mixed Ce-Fe samples as compared to pure Fe_2O_3 , a test reaction with H_2 reduction and CO_2 reoxidation was set up. The samples are reduced in 5% H_2 in Ar during 1 min. By contacting the reduced sample with CO_2 , CO is produced (see eq 2b). The observed space time yield of CO production as a function of time for 20Ce-Fe during the 2nd, 5th, and 10th cycle is displayed in Figure 8. The formation rates pass over sharp maxima in the initial phase of the reaction and then decrease because of the decreasing amount of reduced iron and cerium oxides in the sample. The formation of CO during the 10th cycle was about 5% lower than in the second.

Figure 9 shows the amount of produced CO after the 1st and 10th redox cycle for samples 0 to 100Ce-Fe. In both cycles, the product yield is higher for mixed materials than for pure ones. Especially, the samples 20 to 70Ce-Fe produce over 5 times more CO than Fe_2O_3 , with the highest yield for 20Ce-Fe. The amount of CO produced over CeO_2 was 10 times lower than for Fe_2O_3 . By comparing the yield of the 1st and 10th cycle, stability against sintering can be assessed. For the mixed samples, the amount of the produced CO decreases only

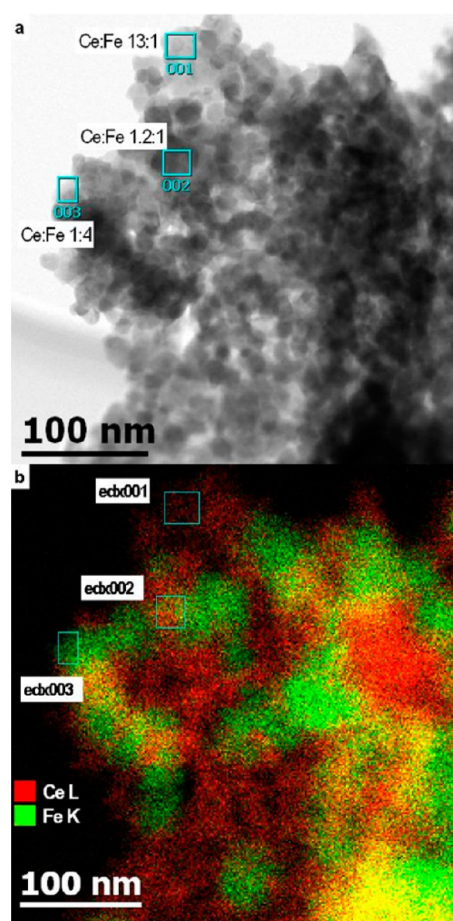


Figure 5. TEM-based results for 50Ce-Fe: (a) STEM BF image with rectangular marks of EDX analysis and Ce to Fe ratios determined from the EDX spectra and (b) EDX elemental mapping of the area shown on (a); separation of ceria from iron oxide is clearly observed.

slightly ($\sim 7\%$) after the 10 redox cycles. In contrast, the single iron oxide loses more than 70% of the initial activity after 10 cycles. 20Ce-Fe retains the highest activity after ten redox cycles, showing this sample has a structure that best withstands deactivation. After cycling, all samples were remeasured in BET. The BET surface areas have decreased compared to those of the fresh materials (see Table 1), indicating that some sintering occurred. In order to understand the better performance of the mixed Ce-Fe samples in chemical looping, in situ structural measurements were performed, both separate reduction and reoxidation as well as complete cycling experiments.

3.4. In Situ XRD during H_2 -TPR. The reduction of pure Fe_2O_3 to metallic iron can be expressed by the following consecutive reaction scheme: $\text{Fe}_2\text{O}_3 \rightarrow \text{Fe}_3\text{O}_4 \rightarrow \text{FeO}_x \rightarrow \text{Fe}$.³⁴ Upon interaction of hydrogen with pure ceria, two stable cerium oxidation states, Ce^{3+} and Ce^{4+} , have been observed.²⁶

Conventional H_2 -TPR of the Ce-Fe samples results in complex profiles involving several reduction peaks as shown in Figure 10a. Table 2 presents the stoichiometric amount of available oxygen in both Fe_2O_3 and CeO_2 , as well as the amount that is removed upon reduction as a result of H_2 -TPR (Figure 10a). For all samples, this amount is less than the total amount available. For 20Ce-Fe, a maximum amount of 93% of oxygen can be removed.

The nature of the TPR peaks can be interpreted combined with in situ XRD, performed with the same ramp rate and

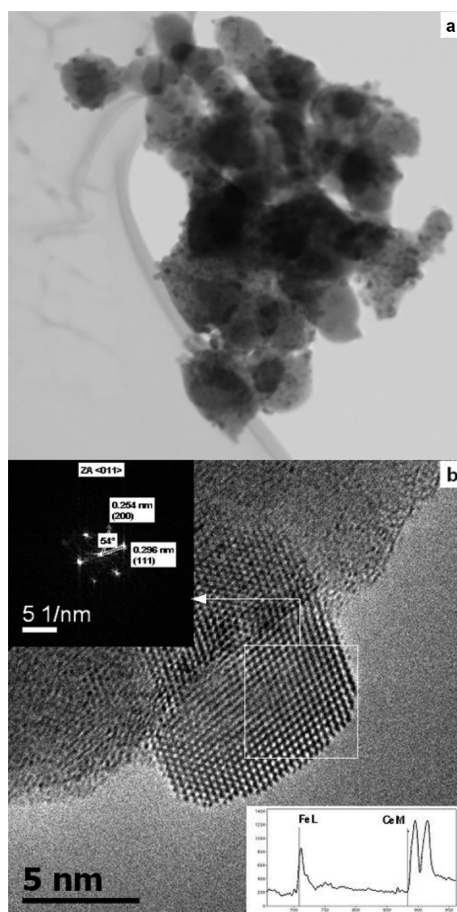


Figure 6. TEM-based results of 20Ce-Fe: (a) STEM BF image; (b) HRTEM image of a single Ce(Fe)O₂ particle with FFT (top left) and EEL spectrum (lower right) taken in the middle of the particle using a 0.5 nm electron probe.

hydrogen concentration and similar flow rate. For the mixed materials, time-resolved XRD during H₂-TPR was performed to interpret their reducibility (Figure 10b–d). For 90Ce-Fe, no Fe₂O₃ diffractions are visible at room temperature, but a weak metal Fe(110) peak does emerge at $\sim 45^\circ$ from $T = 550^\circ$ on. Its appearance can be attributed to sintering of finely distributed Fe₂O₃ nanocrystallites upon TPR, making them detectable in XRD, or to a segregation of Fe from the solid solution during reduction. For 20, 50, and 70Ce-Fe, Fe₂O₃ peaks are visible at room temperature (Figure 10c: 50Ce-Fe; patterns for 70 and 20Ce-Fe are similar, not shown). During reduction, they evolve from 400 °C on into Fe₃O₄ peaks (30.1° (220), 35.5°

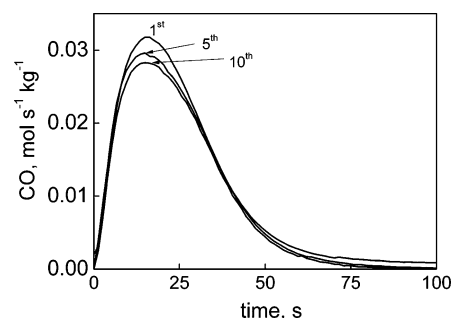


Figure 8. Space time yield of CO during the reoxidation phase with CO₂/He for 20Ce-Fe after 1, 5, and 10 redox cycles.

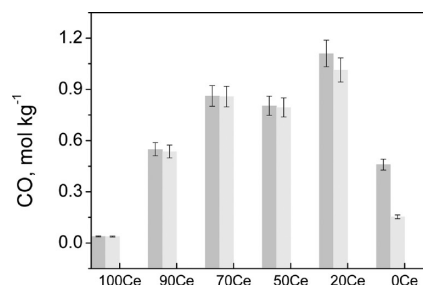


Figure 9. CO produced after the 1st (dark bar) and 10th cycle (light bar) over the xCe-Fe samples. The error bar represents twice the standard deviation.

(311), and 43.1° (400)), further to FeO (36.0° (111) and 41.9° (200)) around 500 °C, and finally into Fe (110) above 550 °C.

Characteristic peaks associated with crystalline CeO₂ appear in all patterns of 100 to 20Ce-Fe and remain visible throughout H₂-TPR. Peaks of the reduced phase Ce₂O₃ are never observed, but a possible partial reduction is checked from the position of the CeO₂(111) diffraction.³⁵ In pure 100Ce-Fe, its position as a function of temperature essentially yields a monotonous slope, reflecting the peak shift due to thermal lattice expansion (Figure 10d). Only at the highest temperature, i.e., close to 800 °C, a downward deviation starts to develop, due to the onset of thermal reduction. At high enough temperature, this process removes O from the lattice, thus changing Ce⁴⁺ into Ce³⁺. As the latter cation is larger than the former, this induces an additional lattice expansion, with a decreasing diffraction angle as a result.³⁵ For the mixed Ce-Fe samples, this thermal reduction is more obvious and starts already around 700 °C. In addition, an extra downward shift is observed in these mixed samples. 90Ce-Fe and 70Ce-Fe start deviating from the straight CeO₂ curve at 300 °C. This

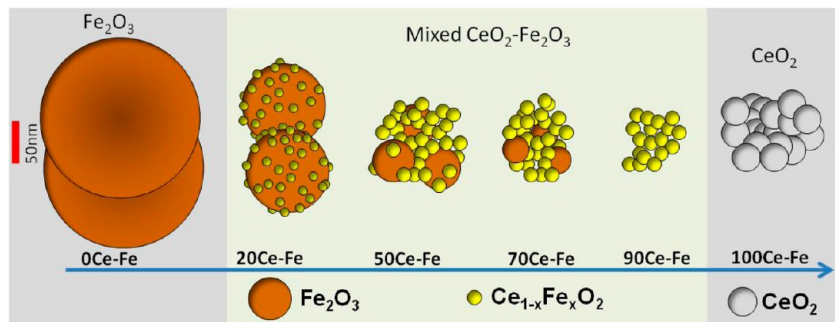


Figure 7. Schematic illustration of mixed CeO₂-Fe₂O₃ samples, based upon ICP composition, XRD patterns, STEM, EDX, and EELS.

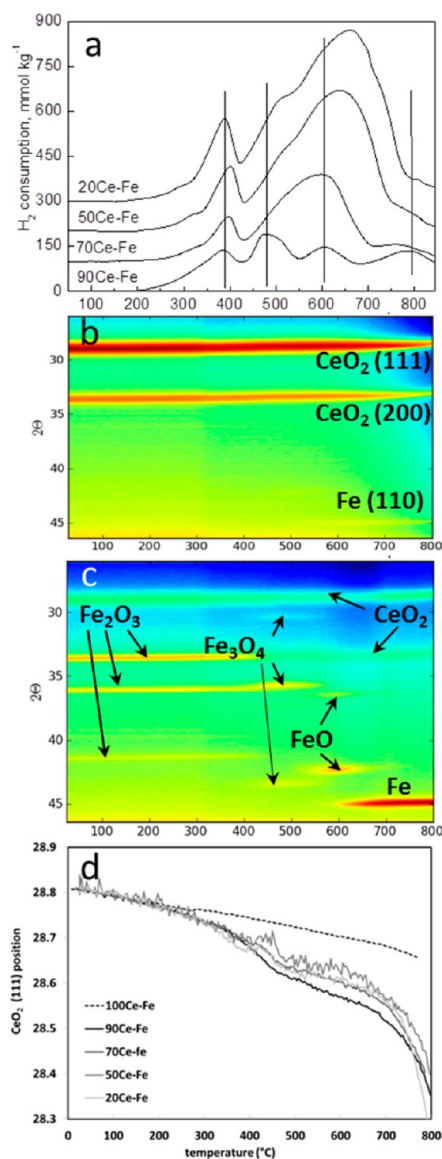


Figure 10. (a) Conventional H₂-TPR of Ce-Fe samples; (b) 2D XRD pattern recorded during H₂-TPR for 90Ce-Fe; (c) 2D XRD pattern recorded during H₂-TPR for 50Ce-Fe; (d) CeO₂(111) position from XRD during H₂-TPR for the Ce-Fe samples. All TPR measuring conditions: 20 °C/min; 5% H₂/He.

Table 2. Amount of Available Oxygen and Oxygen Removable by Reduction

sample	O _{Fe2O3} (mol kg ⁻¹)	O _{CeO2} (mol kg ⁻¹)	O _{Fe2O3} / O _{CeO2}	O _{tot} (mol kg ⁻¹)	O _{red} ^a (mol kg ⁻¹)
100Ce-Fe	0	2.9	0	2.9	1.2
90Ce-Fe	0.9	2.6	0.4	3.5	2.6
70Ce-Fe	2.8	2.0	1.4	4.8	3.8
50Ce-Fe	4.7	1.5	3.2	6.2	5.1
20Ce-Fe	7.5	0.6	12.9	8.1	7.5
0Ce-Fe	9.4	0	—	9.4	8.0

^aAmount of O consumed in H₂-TPR.

indicates that, from this temperature on, part of Ce is already being reduced from 4+ to 3+.

This early reducing part can be a Ce fraction connected to Fe, e.g., in the solid solution. In the curves for 50 and 20Ce-Fe,

the same deviation in position is detected, namely at 300°, but in addition, a short though abrupt downward shift is noted around 450 °C. The latter can correspond to a different type of Ce species being reduced at this temperature, before bulk reduction above 700 °C sets in. Hence, reduction of ceria in mixed 90 to 20Ce-Fe samples starts at lower temperatures than for 100Ce-Fe. On the basis of the TEM characterization, the latter must be ascribed to improved lattice oxygen transfer in the CeO₂ structure in the presence of iron species in the lattice.

With the help of the in situ XRD patterns, the TPR profiles of Figure 10a can be unraveled. Sample 20Ce-Fe shows a three peaks profile similar to the reduction of Fe₂O₃.^{34,36,37} The low temperature peak arises from reduction of Fe₂O₃ to Fe₃O₄, as well as from partial reduction of CeO₂ (Figure 10d). The high-temperature peaks correspond to reduction of Fe₃O₄ to FeO (around 500 °C) and further to Fe (650 °C)³⁴ and to the continuing reduction of CeO₂. However, the amount of oxygen from iron oxide in 20Ce-Fe is thirteen times higher than that from CeO₂ (Table 2), so that the main contribution to the TPR profile stems from reduction of the iron oxide. In 50Ce-Fe, the amount of oxygen from ceria is close to 25% of the total amount present. This sample displays three reduction peaks. The peak at 400 °C corresponds to the phase transition of Fe₂O₃ to Fe₃O₄ and a first partial CeO₂ reduction, while the broad peak at 600 °C reflects the 2-step reduction of Fe₃O₄ to Fe and a continuing reduction of CeO₂. According to the in situ XRD results, the high temperature peak (750 °C) can be attributed to bulk reduction of CeO₂ only. In 70 and 90Ce-Fe, the amount of oxygen from CeO₂ and Fe₂O₃ is comparable and both samples display four reduction peaks. For 70Ce-Fe, identification of TPR with in situ XRD yields H₂ consumption peaks related to iron oxide phase transitions around 400, 500, and 600 °C. On the basis of the evolution of the CeO₂ peak position for this sample (Figure 10d), the 400 °C TPR peak will contain a significant contribution from partial CeO₂ reduction, while the TPR peak around 800 °C is related to bulk CeO₂ reduction. As to the 90Ce-Fe sample, no XRD peaks related to FeO_x are observed until metal Fe emerges above 550 °C. On the other hand, the evolution of the CeO₂ peak position with temperature again implies a partial ceria reduction around 400 °C and a bulk reduction above 700 °C, which can already account for the lower and higher temperature TPR peaks. The TPR profile further indicates that distinct reduction occurs also at 500 and 600 °C. On the basis of the similarity of the TPR profiles for 70 and 90Ce-Fe, with 4 consumption peaks each, the middle temperature peaks should then relate to iron oxide reduction, albeit for nanocrystallites smaller than 3 nm or for iron incorporated into the ceria crystallites, as indicated by TEM and EDX.

3.5. In Situ XRD during CO₂-TPO. The oxidation reaction of Fe and CeO_{2-x} can run through stages opposite to those involved in the reduction:



The further oxidation of Fe₃O₄ to Fe₂O₃ can only be achieved by application of gaseous oxygen.³⁴ Therefore, once the freshly prepared material underwent a reduction-reoxidation cycle, the iron oxide with highest attainable oxygen content is Fe₃O₄.

Figure 11a shows the conventional TPO profiles for the reduced samples, performed immediately after cool down from

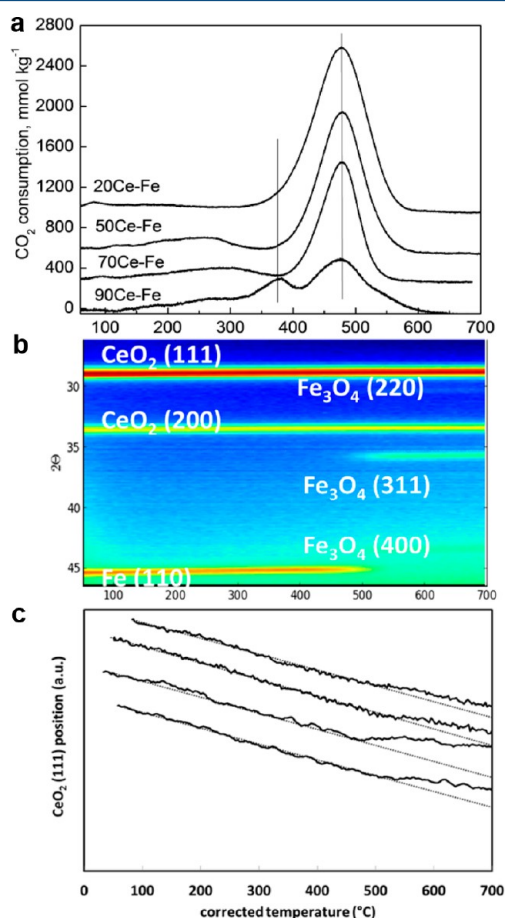


Figure 11. (a) Conventional CO_2 -TPO of Ce-Fe samples; (b) 2D XRD pattern recorded during CO_2 -TPO for 70Ce-Fe; (c) $\text{CeO}_2(111)$ position from XRD during CO_2 -TPO for the $x\text{Ce-Fe}$ samples. All TPO measuring conditions: 20 °C/min, CO_2 .

the H_2 -TPR. All samples display a major CO_2 consumption peak around 475 °C. On the basis of Figure 11b,c, the latter corresponds to a combination of phase transition of Fe into Fe_3O_4 and reoxidation of the partially reduced CeO_2 . The dominating contribution depends on the ratio of CeO_2 to Fe_2O_3 . The CO_2 -TPO profile for 90Ce-Fe presented an additional peak at 400 °C suggesting the presence of a second reoxidation process, e.g., of the mixed Ce-Fe phase, next to the reoxidation of bulk CeO_2 at 475 °C. Time resolved in situ XRD data during CO_2 -TPO for all Ce-Fe samples show the characteristic Fe diffraction, which gives way to diffraction peaks of Fe_3O_4 . An example is depicted in Figure 11b. The temperature at which the phase transition occurs increases with increasing iron oxide content from 475 °C for 90Ce-Fe up to 525 °C for 50 and 20Ce-Fe. No intermediate FeO phase is apparent. Formation of FeO strongly depends on reaction temperature and gas composition.

Figure 12 shows the equilibrium gas composition of the iron-carbon-oxygen system at different temperatures using thermodynamic data from Barin.³⁸ Under the present reaction conditions, the oxidation reaction proceeds by direct conversion of Fe into Fe_3O_4 . The $\text{CeO}_2(111)$ diffraction during TPO of the mixed Ce-Fe samples starts at a position

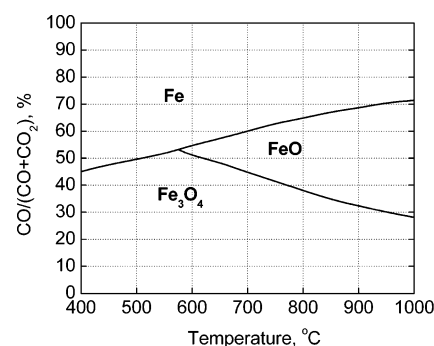


Figure 12. Equilibrium lines of the systems CO/CO_2 over iron/iron oxide.

corresponding to partially reduced CeO_2 and shows the typical linear downward shift corresponding to thermal expansion (Figure 11c). In addition, an increase in position occurs for all samples around 500 °C indicating reoxidation of Ce^{3+} to Ce^{4+} takes place.

3.6. In Situ Redox Cycle XRD Experiments. The cycling experiments at 600 °C show the evolution of the different phases throughout repeated reduction and oxidation. In each reoxidation, the XRD intensity increases due to enhanced scattering by the CO_2 atmosphere, giving rise to a higher background intensity.

The 2D diffraction pattern for the 90Ce-Fe sample shows mainly CeO_2 diffractions. In the first half-cycle, the pattern starts without any iron oxide diffraction but a faint Fe diffraction appears after a 100 s reduction and remains visible until 700 s when the oxidizing pulse starts (Figure 13a). During the oxidation process, the Fe diffraction gives way to a weak

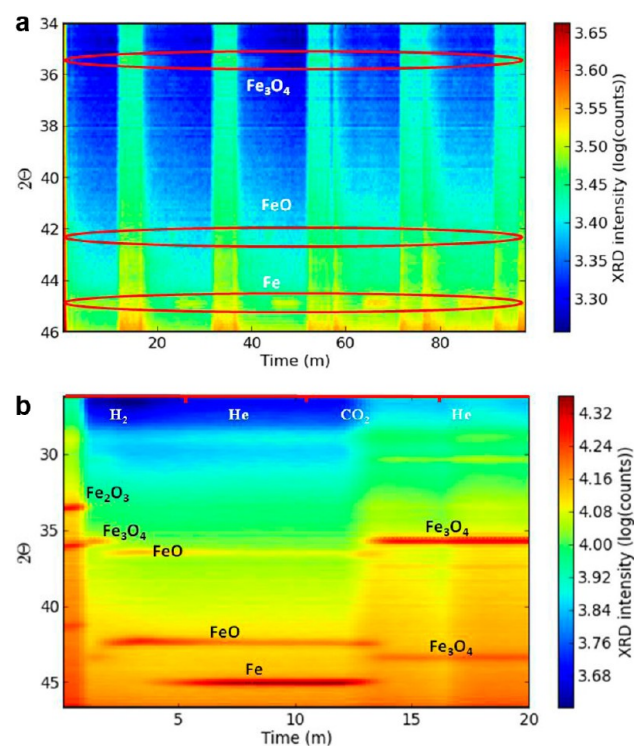


Figure 13. (a) Time-resolved in situ XRD patterns during 5 redox cycles at 600° of 90Ce-Fe; (b) time-resolved in situ XRD patterns during 1st redox cycle at 600° for 20Ce-Fe.

Fe_3O_4 diffraction (35.5°), which persists until the end of the purging (~ 1300 s). This pattern is repeated during consecutive cycles, except that, from the second cycle on, the appearance of the Fe diffraction upon reduction is preceded by a faint and short line originating from FeO (42° , ~ 1400 s). The first reduction is hence necessary to have Fe emerge as a distinct crystallographic phase and from there on.

70Ce–Fe behaves very much the same as 90Ce–Fe does, with the exception that Fe_2O_3 diffractions are now present from the start (not shown). Upon reduction, these are replaced by diffractions of Fe_3O_4 after 50 s, then FeO around 100 s, and finally Fe from 200 s on as single reduced phase. Upon reoxidation, FeO reappears for a short 30 s before giving way to Fe_3O_4 . This indicates that oxidation conditions in the present cycle do allow for FeO to appear in the XRD pattern. In the following cycles, the reduction starts from Fe_3O_4 and is less deep so that FeO can remain present next to Fe in the reduction half-cycles.

Reduction of 50Ce–Fe never leads to a single phase. Rather, both FeO and Fe remain present at the end of each reducing half-cycle (Figure 13b). The 5 min reduction time is thus not sufficient to reduce all of the iron oxide completely to the metallic state. This can be related to the changed composition of this sample: according to TEM, 50Ce–Fe contains both Fe_2O_3 and CeO_2 with incorporated iron as two separate phases with crystallites of similar morphology and size. The larger crystallites of Fe_2O_3 are more difficult to reduce completely. In oxidizing half-cycles, the FeO diffractions first gain intensity at the expense of Fe and then quickly give way to Fe_3O_4 (Figure 13b), which pertain until the end of purging. For 20Ce–Fe, the findings of 50Ce–Fe essentially hold: deepest reduction in the first cycle, but incomplete, and reoxidation to Fe_3O_4 with short reappearance of FeO (not shown).

In order to assess the behavior of the compounds during cycling, the peak widths and positions of characteristic diffractions for iron, iron oxide, and ceria have been determined by fitting a Gaussian function to the diffraction. On the basis of the Scherrer equation, the width of the peak correlates with the crystallite size, while the peak position reflects the lattice unit cell size through the Bragg law. In all samples, the CeO_2 (111) peak width changed according to the same pattern: a fast decrease in the first cycle is followed by a slower steady decrease in the subsequent cycles (see Figure 14a).

The narrowing peak indicates that the ceria crystallites are growing larger as the cycling proceeds. The same exercise is made for diffractions of Fe_3O_4 (311): the peak width decreases slightly over the 5 cycling periods, corresponding to a small crystallite size increase (Figure 14b), except for 90Ce–Fe, where diffractions are weak and no clear trend is observed. Thus, both CeO_2 and Fe_3O_4 suffer from some sintering during cycling, which can account for the small loss in activity as evidenced by the stability plot (Figure 9).

For samples 20 to 70Ce–Fe, the CeO_2 (111) position as a function of cycles shows at first a steep drop-off due to thermal lattice expansion, during rapid heating to 600°C , followed by a periodic variation (Figure 14a). In reducing conditions, the position is lower by 0.02° , corresponding to a larger lattice size, than in the oxidizing atmosphere. This is due to partial ceria reduction, making the lattice expand as Ce^{3+} which is larger than Ce^{4+} , and agrees with the 600°C cycling temperature and the TPR data (Figure 10d). For 90Ce–Fe, this pattern does not occur and no straightforward trend could be established in the CeO_2 (111) position. As to the iron related peaks (Figure 14b),

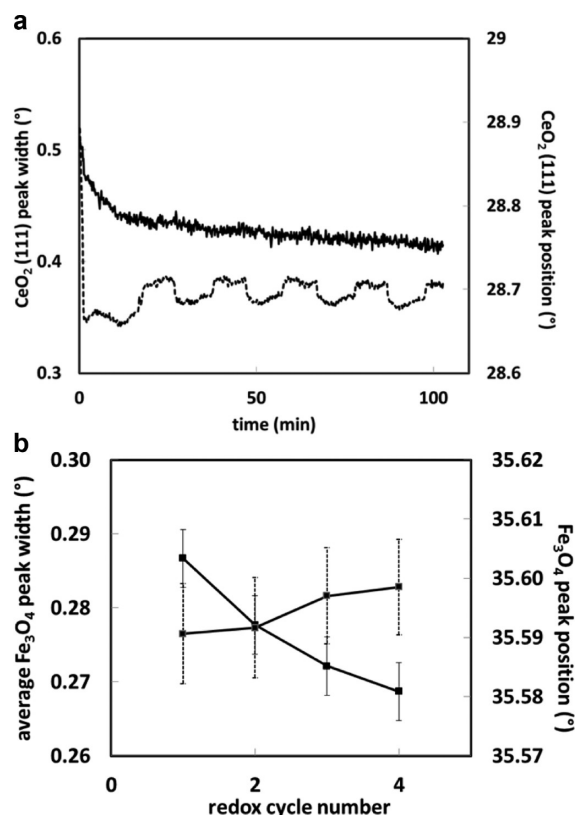


Figure 14. (a) Shift of CeO_2 (111) peak width (solid line) and position (dashed line) with cycling time in 70Ce–Fe; (b) shift of Fe_3O_4 peak width (solid line) and (110) peak position (dashed line) with number of cycle for sample 70Ce–Fe.

the position of the Fe_3O_4 (311) peak remains constant at $\sim 35.6^\circ$ throughout all CO_2 and He purge half-cycles for all samples, indicating a stable unit cell size. During reduction and consecutive purging, FeO lines appear and tend to shift to higher diffraction angle toward the end of the half-cycle. The latter can be related to an ongoing reduction, which gives rise to a shrinking lattice constant.

4. CONCLUSIONS

A series of CeO_2 – Fe_2O_3 materials with 0, 20, 50, 70, 90, and 100 wt % CeO_2 was prepared for use as oxygen storage material in the chemical looping process for CO_2 conversion. The mixed materials contain a solid solution of ceria with incorporated iron and a separate Fe_2O_3 phase below 70 wt % CeO_2 . In all mixed CeO_2 – Fe_2O_3 samples, the crystallite size of the solid solution was considerably smaller compared to pure CeO_2 .

The generation of CO from CO_2 through H_2 – CO_2 redox cycles was investigated isothermally to evaluate the effect of CeO_2 upon Fe_2O_3 . The total amount of evolved CO of the CeO_2 promoted Fe_2O_3 samples was always higher than for pure Fe_2O_3 and remained so during ten repeated redox cycles. Hence, the addition of CeO_2 to the iron oxide preserved their activity by suppressed sintering of iron oxide. The CO yield over 20Ce–Fe was twice as high as for pure Fe_2O_3 , and only a small loss in activity was noted after 10 cycles. 50 and 70Ce–Fe equally showed improved performance and high stability. By means of in situ XRD measurements in H_2 -TPR, CO_2 -TPO, and redox cycling, the participation of CeO_2 in the redox process was assessed. In a 90 wt % CeO_2 – Fe_2O_3 sample, no iron related diffractions were present at the start, but the H_2 -

TPR treatment made Fe appear as phase segregating from ceria. For lower CeO₂ loadings, mixed Ce–Fe samples underwent in H₂-TPR a stepwise reduction to metal Fe around 400 °C. Even before this temperature, a partial reduction of the CeO₂ solid solution was noted although the reduced Ce₂O₃ phase was not reached. CO₂ reoxidation of the solid solution started at 450 °C, whereas Fe was reoxidized directly to Fe₃O₄ around 500 °C. Compared to the pure compounds CeO₂ and Fe₂O₃, the mixed CeO₂–Fe₂O₃ samples yield improved activity. Moreover, the combination of both oxides efficiently suppressed the sintering effect, resulting in improved stability in chemical looping processes.

AUTHOR INFORMATION

Corresponding Author

*E-mail: Vladimir.Galvita@UGent.be. Tel: +32 9 264.45.21. Fax: +32 9 264.49.99.

Notes

The authors declare no competing financial interest.

ACKNOWLEDGMENTS

This work was supported by the “Long Term Structural Methusalem Funding by the Flemish Government”, the Fund for Scientific Research Flanders (FWO, project number 3G004613), and the Interuniversity Attraction Poles Programme, IAP7/5, Belgian State – Belgian Science Policy.

REFERENCES

- (1) Agency, I. E. *World energy outlook*; OECD/IEA: Paris, France, 2012.
- (2) Adanez, J.; Abad, A.; Garcia-Labiano, F.; Gayan, P.; de Diego, L. F. Progress in chemical-looping combustion and reforming technologies. *Prog. Energy Combust. Sci.* **2012**, *38* (2), 215–282.
- (3) Fan, L.-S.; Li, F. Chemical looping technology and its fossil energy conversion applications. *Ind. Eng. Chem. Res.* **2010**, *49* (21), 10200–10211.
- (4) Luo, C.; Zheng, Y.; Ding, N.; Wu, Q.; Bian, G.; Zheng, C. Development and performance of CaO/La₂O₃ sorbents during calcium looping cycles for CO₂ capture. *Ind. Eng. Chem. Res.* **2010**, *49* (22), 11778–11784.
- (5) Ryden, M.; Arjmand, M. Continuous hydrogen production via the steam-iron reaction by chemical looping in a circulating fluidized-bed reactor. *Int. J. Hydrogen Energy* **2012**, *37* (6), 4843–4854.
- (6) Galvita, V.; Messerle, V. E.; Ustimenko, A. B. Hydrogen production by coal plasma gasification for fuel cell technology. *Int. J. Hydrogen Energy* **2007**, *32* (16), 3899–3906.
- (7) Abanades, S. CO₂ and H₂O reduction by solar thermochemical looping using SnO₂/SnO redox reactions: Thermogravimetric analysis. *Int. J. Hydrogen Energy* **2012**, *37* (10), 8223–8231.
- (8) Chiron, F.-X.; Patience, G. S.; Riffart, S. Hydrogen production through chemical looping using NiO/NiAl₂O₄ as oxygen carrier. *Chem. Eng. Sci.* **2011**, *66* (24), 6324–6330.
- (9) Sim, A.; Cant, N. W.; Trimm, D. L. Ceria-zirconia stabilised tungsten oxides for the production of hydrogen by the methane-water redox cycle. *Int. J. Hydrogen Energy* **2010**, *35* (17), 8953–8961.
- (10) Galvita, V. V.; Poelman, H.; Marin, G. B. Hydrogen production from methane and carbon dioxide by catalyst-assisted chemical looping. *Top. Catal.* **2011**, *54* (13–15), 907–913.
- (11) Liu, X.; Wang, H. Hydrogen production from water decomposition by redox of Fe₂O₃ modified with single- or double-metal additives. *J. Solid State Chem.* **2010**, *183* (5), 1075–1082.
- (12) Solunke, R. D.; Vesper, G. Hydrogen production via chemical looping steam reforming in a periodically operated fixed-bed reactor. *Ind. Eng. Chem. Res.* **2010**, *49* (21), 11037–11044.
- (13) Najera, M.; Solunke, R.; Gardner, T.; Vesper, G. Carbon capture and utilization via chemical looping dry reforming. *Chem. Eng. Res. Des.* **2011**, *89* (9), 1533–1543.
- (14) Scheffe, J. R.; Allendorf, M. D.; Coker, E. N.; Jacobs, B. W.; McDaniel, A. H.; Weimer, A. W. Hydrogen production via chemical looping redox cycles using atomic layer deposition-synthesized iron oxide and cobalt ferrites. *Chem. Mater.* **2011**, *23* (8), 2030–2038.
- (15) Loutzenhiser, P. G.; Galvez, M. E.; Hischer, I.; Stamatou, A.; Frei, A.; Steinfeld, A. CO₂ splitting via two-step solar thermochemical cycles with Zn/ZnO and FeO/Fe₃O₄ redox reactions II: Kinetic analysis. *Energy Fuels* **2009**, *23* (5), 2832–2839.
- (16) Galvita, V.; Hempel, T.; Lorenz, H.; Rihko-Struckmann, L. K.; Sundmacher, K. Deactivation of modified iron oxide materials in the cyclic water gas shift process for CO-free hydrogen production. *Ind. Eng. Chem. Res.* **2008**, *47* (2), 303–310.
- (17) Otsuka, K.; Yamada, C.; Kaburagi, T.; Takenaka, S. Hydrogen storage and production by redox of iron oxide for polymer electrolyte fuel cell vehicles. *Int. J. Hydrogen Energy* **2003**, *28* (3), 335–342.
- (18) Yamaguchi, D.; Tang, L.; Wong, L.; Burke, N.; Trimm, D.; Nguyen, K.; Chiang, K. Hydrogen production through methane-steam cyclic redox processes with iron-based metal oxides. *Int. J. Hydrogen Energy* **2011**, *36* (11), 6646–6656.
- (19) Chen, S.; Shi, Q.; Xue, Z.; Sun, X.; Xiang, W. Experimental investigation of chemical-looping hydrogen generation using Al₂O₃ or TiO₂-supported iron oxides in a batch fluidized bed. *Int. J. Hydrogen Energy* **2011**, *36* (15), 8915–8926.
- (20) Sahoo, S. K.; Mohapatra, M.; Pandey, B.; Verma, H. C.; Das, R. P.; Anand, S. Preparation and characterization of Fe₂O₃-CeO₂ composite. *Mater. Charact.* **2009**, *60* (5), 425–431.
- (21) Padeste, C.; Cant, N.; Trimm, D. The influence of water on the reduction and reoxidation of ceria. *Catal. Lett.* **1993**, *18* (3), 305–316.
- (22) Zhu, T.; Kundakovic, L.; Dreher, A.; Flytzani-Stephanopoulos, M. Redox chemistry over CeO₂-based catalysts: SO₂ reduction by CO or CH₄. *Catal. Today* **1999**, *50* (2), 381–397.
- (23) Hedayati, A.; Azad, A.-M.; Ryden, M.; Leion, H.; Mattisson, T. Evaluation of novel ceria-supported metal oxides as oxygen carriers for chemical-looping combustion. *Ind. Eng. Chem. Res.* **2012**, *51* (39), 12796–12806.
- (24) Menon, U.; Poelman, H.; Bliznuk, V.; Galvita, V. V.; Poelman, D.; Marin, G. B. Nature of the active sites for the total oxidation of toluene by CuO/CeO₂/Al₂O₃. *J. Catal.* **2012**, *295* (0), 91–103.
- (25) Staudt, T.; Lykhach, Y.; Tsud, N.; Skala, T.; Prince, K. C.; Matolin, V.; Libuda, J. Ceria reoxidation by CO₂: A model study. *J. Catal.* **2010**, *275* (1), 181–185.
- (26) Trovarelli, A. *Catalysis by Ceria and Related Materials*; Imperial College Press: London, 2002; Vol. 2.
- (27) Gupta, A.; Kumar, A.; Waghmare, U. V.; Hegde, M. S. Origin of activation of lattice oxygen and synergistic interaction in bimetal-ionic Ce_{0.89}Fe_{0.1}Pd_{0.01}O₂ catalyst. *Chem. Mater.* **2009**, *21* (20), 4880–4891.
- (28) Perez-Alonso, F. J.; Lopez Granados, M.; Ojeda, M.; Terreros, P.; Rojas, S.; Herranz, T.; Fierro, J. L. G.; Gracia, M.; Gancedo, J. R. Chemical structures of coprecipitated Fe-Ce mixed oxides. *Chem. Mater.* **2005**, *17* (9), 2329–2339.
- (29) Gupta, A.; Waghmare, U. V.; Hegde, M. S. Correlation of oxygen storage capacity and structural distortion in transition-metal-, noble-metal-, and rare-earth-ion-substituted CeO₂ from first principles calculation. *Chem. Mater.* **2010**, *22* (18), 5184–5198.
- (30) Scherrer, P. *Nachr. Ges. Wiss. Göttingen* **1918**, *26*, 98–100.
- (31) Niemantsverdriet, J. W. *Spectroscopy in Catalysis*; Wiley: Weinheim, 2007.
- (32) Perez-Alonso, F. J.; Melian-Cabrera, I.; Lopez Granados, M.; Kapteijn, F.; Fierro, J. L. G. Synergy of Fe/Ce_{1-x}O₂ mixed oxides for N₂O decomposition. *J. Catal.* **2006**, *239* (2), 340–346.
- (33) Pakharukova, V. P.; Moroz, E. M.; Kriventsov, V. V.; Zyuzin, D. A.; Kosmambetova, G. R.; Strizhak, P. E. Copper-cerium oxide catalysts supported on monoclinic zirconia: Structural features and catalytic behavior in preferential oxidation of carbon monoxide in hydrogen excess. *Appl. Catal., A: Gen.* **2009**, *365* (2), 159–164.

- (34) Zielinski, J.; Zglinicka, I.; Znak, L.; Kaszkur, Z. Reduction of Fe₂O₃ with hydrogen. *Appl. Catal., A: Gen.* **2010**, *381* (1–2), 191–196.
- (35) Galvita, V. V.; Poelman, H.; Rampelberg, G.; De Schutter, B.; Detavernier, C.; Marin, G. B. Structural and kinetic study of the reduction of CuO-CeO₂/Al₂O₃ by time-resolved X-ray diffraction. *Catal. Lett.* **2012**, *142* (8), 959–968.
- (36) Lin, H.-Y.; Chen, Y.-W.; Li, C. The mechanism of reduction of iron oxide by hydrogen. *Thermochim. Acta* **2003**, *400* (1–2), 61–67.
- (37) Li, K.; Haneda, M.; Gu, Z.; Wang, H.; Ozawa, M. Modification of CeO₂ on the redox property of Fe₂O₃. *Mater. Lett.* **2013**, *93* (0), 129–132.
- (38) Barin, L.; Knacke, O. *Thermochemical Properties of Inorganic Substance*; Springer-Verlag: New York, 1973.